Multiple lobes in the far-field distribution of terahertz quantum-cascade lasers due to self-interference

B. Röben,[a] M. Wienold,[b] L. Schrottke, and H. T. Grahn
Paul-Drude-Institut für Festkörperelektronik, Leibniz-Institut im Forschungsverbund Berlin e. V., Hausvogteiplatz 5–7, 10117 Berlin, Germany

(Received 11 April 2016; accepted 27 May 2016; published online 6 June 2016)

The far-field distribution of the emission intensity of terahertz (THz) quantum-cascade lasers (QCLs) frequently exhibits multiple lobes instead of a single-lobed Gaussian distribution. We show that such multiple lobes can result from self-interference related to the typically large beam divergence of THz QCLs and the presence of an inevitable cryogenic operation environment including optical windows. We develop a quantitative model to reproduce the multiple lobes. We also demonstrate how a single-lobed far-field distribution can be achieved.
[http://dx.doi.org/10.1063/1.4953596]

Terahertz (THz) quantum-cascade lasers (QCLs) are powerful radiation sources which have attracted much interest for applications in imaging[1–4] and spectroscopy.[5–9] Many of these applications benefit from or even require a far-field distribution of the emission intensity which is as close as possible to a Gaussian profile. However, multiple lobes have frequently been reported for THz QCLs both with metal-metal and single-plasmon (SP) waveguides. In the case of metal-metal waveguides, it has been shown that the modulations in the far-field distribution appear due to interference of the radiation emitted from the front facet with diffracted radiation from the back facet.[10,11] For SP waveguides, there are a number of different mechanisms that have been discussed in the literature. A similar effect as for metal-metal waveguides[12] or an aperture-like diffraction effect due to the wavelength-sized waveguide mode[13] may be the origin. In addition, further explanations include the presence of the substrate[14,15] and reflections within or between cryostat windows.[14] The diversity of the suggested explanations in the literature clearly shows that a thorough investigation of the phenomenon is lacking, in particular for SP waveguides.

In this letter, we present a detailed study of the origin of the multiple lobes in the far-field distribution of THz QCLs with SP waveguides. We measured the far-field distribution and developed an analytical model for its calculation. From a comparison of the measured and the calculated far-field distributions, the mechanism leading to the modulations can be unambiguously identified. We further employ the model to investigate the influence of several parameters on the far-field distribution. Finally, we present a method to suppress the modulations.

The operation of THz QCLs is up to now restricted to temperatures below 200 K. Therefore, a cooling system has always to be used. For our measurements, we employed a Stirling cooler, which contains a polypropylene foil window with a thickness of 75 μm and a clear aperture of 32 mm, through which the emitted THz radiation is transmitted. The THz QCLs[16,17] are based on single-plasmon waveguides and Fabry-Pérot resonators. The QCL chips are indium-soldered on gold-plated copper submounts.

[a]Author to whom correspondence should be addressed. Electronic mail: roeben@pdi-berlin.de
[b]Present address: Deutsches Zentrum für Luft- und Raumfahrt, Rutherfordstr. 2, 12489 Berlin, Germany.

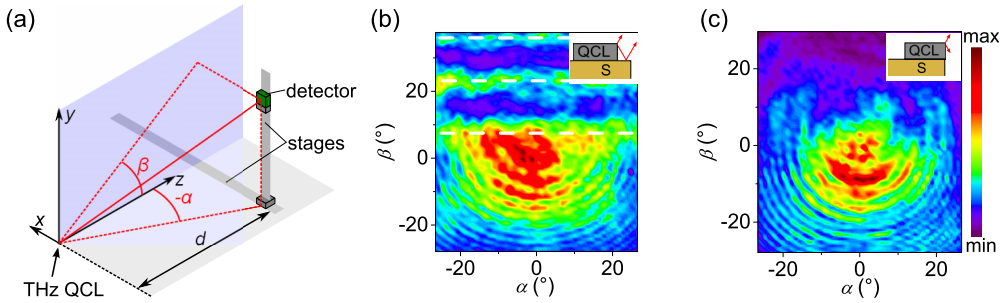

FIG. 1. (a) Schematic diagram of the detection setup. The front facet of the THz QCL is aligned with the x-y plane. (b) Far-field distribution of a THz QCL mounted with a distance of 680 μm to the submount edge. The intensity modulation with a large periodicity is indicated by the white dashed lines. Inset: Schematic of the mounting setup. S: submount. (c) Far-field distribution of a THz QCL mounted aligned with the submount edge. For (b) and (c), we used a single-mode QCL emitting at 2.5 THz and a distance of the detector from the QCL of d = 100 mm.

Figure 1(a) depicts the detection setup and defines the angles used. A single-pixel pyroelectric detector with a chip size of 2×2 mm^2 is scanned along the x-y plane at a distance d from the QCL front facet using two perpendicular motorized translation stages. Figure 1(b) shows the measured far-field distribution for a THz QCL mounted at a distance of 680 μm from the submount edge. Two types of intensity modulations are observed, which differ in their value of the periodicity. The large-periodicity modulation indicated by the horizontal dashed lines is due to interference between radiation directly emitted from the laser with radiation reflected at the submount. Therefore, the large-periodicity modulations disappear, if a THz QCL is aligned with the submount edge as shown in Fig. 1(c). For both configurations, we used a single-mode QCL emitting at 2.5 THz (wavelength λ of 120 μm). We conclude that the presence of the uncovered surface of the metal submount in front of the QCL in Fig. 1(b) is responsible for the large-periodicity modulation. Note that the asymmetry of the far-field distribution in the vertical direction in Figs. 1(b) and 1(c) is due to the asymmetric structure of the SP waveguide.

For the remainder of the letter, we will focus on the modulation with the small periodicity, which is present in both Figs. 1(b) and 1(c), and refer to it as the submount-independent modulation (SIM). Measurements of the far-field distribution for QCLs with a width of 150 μm and lengths of 1.01, 1.34, as well as 1.87 mm and with a length of 1.01 mm and widths of 120, 150, as well as 200 μm mounted aligned with the submount edge showed that the periodicity for the SIM is independent of the ridge width and length. Thus, we can exclude an effect of diffracted radiation from the back facet similar to the effect observed for THz QCLs with metal-metal waveguides, because in this case the periodicity of the modulation should strongly depend on the ridge length. More generally, the SIM is unlikely to originate from the QCL itself. Another possible explanation for the SIM could be reflections within the window of the Stirling cooler. However, the reflectance of the window for angles of incidence between 0° and 40° determined by using a Fourier transform infrared spectrometer (FTIR) exhibits a much larger periodicity than the observed SIM in the far-field distribution so that we can also exclude reflections within the window as the origin of the SIM.

Figure 2 illustrates that radiation reflected from the window of the cooling system can experience an additional reflection at the submount/cold finger. The superposition of the radiation, which is directly transmitted through the window, and the reflected radiation results in constructive or destructive interference depending on the considered angle β with the z-axis. Experimentally, we find a strong influence of the distance a between the QCL and the window of the cooling system on the period of the SIM in the far-field distribution, which decreases with increasing a as shown in the left panels of Figs. 3(a), 3(b), and 3(c).

In order to calculate the far-field distributions, assuming a Gaussian beam seems natural at first glance. However, the Gaussian beam, which is a solution of the paraxial Helmholtz equation, cannot correctly describe radiation with divergence angles of about 40° as it is the case for THz QCLs. In contrast, a spherical wave should approximate divergent radiation much better, but it totally lacks

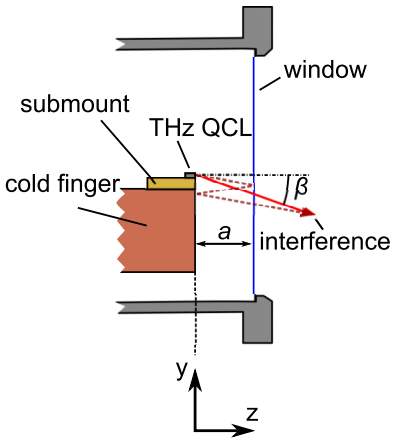

FIG. 2. Schematic diagram of the mechanism leading to the SIM in the far-field distribution showing a section through the QCL mounted in a cooling system. The SIM originates from interference of radiation directly transmitted through the window (solid line) and radiation reflected at the window and the metal submount/cold finger (dashed line).

the directionality which radiation from the THz QCLs with single-plasmon waveguides clearly possess. Therefore, a combination of both models is used. From the equation of the Gaussian beam in Ref. 18, the amplitude and lateral intensity distribution are used, while the part responsible for the phase is replaced by the expression for a spherical wave. Assuming that the front facet is situated at the origin of the coordinate system, the complex amplitude of the emitted radiation at point (x, y, z) is given by

$$F_\theta(x,y,z) = \frac{1}{W_\theta(z)} \exp\left[-\frac{\rho^2}{W_\theta^2(z)} + i\frac{2\pi r}{\lambda}\right], \tag{1}$$

where

$$W_\theta(z) = \sqrt{z^2\theta^2 + \frac{\lambda^2}{\pi^2\theta^2}}, \tag{2}$$

denotes the beam width, $\rho = \sqrt{x^2 + y^2}$, and $r = \sqrt{\rho^2 + z^2}$. The parameter θ denotes the divergence angle in radians.

We employ image theory[19] to calculate the radiation field resulting from the reflection. If a radiation field originating from a source in front of a reflecting surface is considered, the reflected radiation can be thought of to originate from a source on the other side of the reflecting surface.

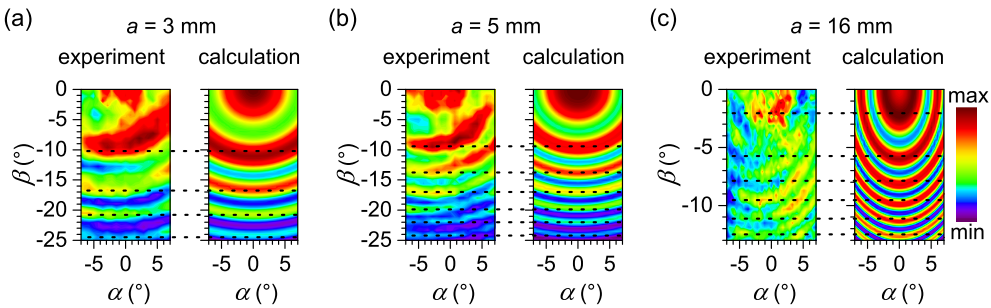

FIG. 3. Comparison of the measured far-field distributions with the respective simulation results of a 2.5-THz single-mode QCL for the distances a of (a) 3, (b) 5, and (c) 16 mm. The error for the measurement of a is 1 mm. The detector distances d used in the measurements are 148, 150, and 300 mm, respectively. The values for a assumed in the calculations are 2.69, 4.32, and 15.25 mm, respectively.

Using this principle, the radiation field resulting from the reflections at the window and the submount/cold finger can be derived from the original radiation field by a translation of $-2a$ along the z-direction. In all calculations, we assume a reflectance of 1 at the submount/cold finger and a reflectance R of 0.04 at the cryostat window, which has been determined by FTIR measurements. Multiple reflections are neglected. For simplicity, we neglected any angular dependence of R. The intensity distribution arising at the detector plane resulting from the interference between the directly emitted radiation and the radiation field from the reflections is then given by

$$I_{\theta,R}(x,y,d) = |\sqrt{1-R}\,F_\theta(x,y,d) + \sqrt{R(1-R)}\,F_\theta(x,y,d+2a)|^2\,, \tag{3}$$

where $x = d\,\tan(\alpha)$ and $y = d\,\tan(\beta)$.

Figure 3 compares the calculated results of the far-field distribution for three different distances a between the QCL and the window with the corresponding experimental results for $\nu = 2.5$ THz ($\lambda = 120$ μm). The value of the divergence angle θ was adjusted to 34° for all values of a. The variation in the periodicity and in the relative peak intensities are well reproduced for the different values of a within the experimental accuracy of determining a.

The far-field distribution is extremely sensitive to small variations in a and λ. As an example, Fig. 4(a) shows a calculated profile of the far-field distribution for $\lambda = 120$ μm ($\nu = 2.5$ THz) and $a = 3$ mm. As shown in Fig. 4(b), a different profile with a phase shift of about π with respect to Fig. 4(a) is obtained when a is increased by only 0.03 mm. The origin of this shift is related to constructive and destructive interference in the direction along the z-axis (α and $\beta = 0°$). The intensity along the z-axis depends on the ratio

$$M = \frac{2a}{\lambda}\,, \tag{4}$$

where $M = 1, 2, \ldots$ for an intensity maximum and $M = 1/2, 3/2, \ldots$ for an intensity minimum, which can be derived from Eq. (3). The profile of the far-field distribution shown in Fig. 4(a) exhibits a maximum at $\beta = 0°$, since $M = 50$ for $a = 3$ mm and $\lambda = 120$ μm according to Eq. (4) and is thus an integer. In contrast, a minimum is observed at $\beta = 0°$ for the profile displayed by the solid line in Fig. 4(b), because the value of a has been changed to 3.03 mm so that $M = 50.5$, which is an odd multiple of 1/2. The profile of the far-field distribution changes in the same manner, if for $a = 3$ mm the wavelength λ is changed from 120 μm as used for the solid line in Fig. 4(a) to 118.81 μm as used for the dashed line in Fig. 4(b), keeping M constant. Since the value for λ or a is only slightly changed, the profiles appear to be identical. However, profiles for larger differences in λ or a keeping M constant may differ significantly at larger negative values of β.

The high sensitivity of the far-field distribution on the wavelength has an important consequence for QCLs in multi-mode operation. While every mode creates a far-field distribution with

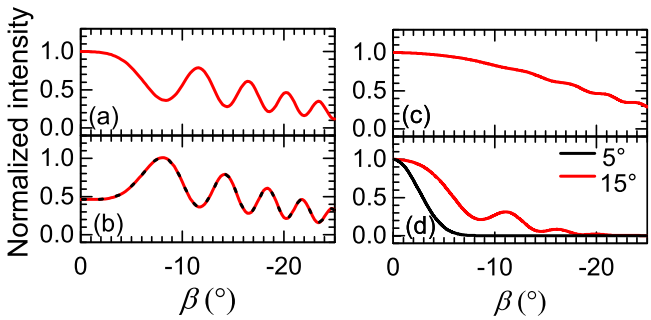

FIG. 4. Profiles of the calculated far-field distributions for $\alpha = 0°$ at a distance $d = 150$ mm. (a) Profile for $a = 3$ mm, $\lambda = 120$ μm, and a divergence angle $\theta = 34°$. (b) Profile for $a = 3.03$ mm and $\lambda = 120$ μm (solid line) as well as $a = 3$ mm and $\lambda = 118.81$ μm (dashed line) both for $\theta = 34°$. The normalization of the intensity in (a) and (b) is identical. (c) Sum of the profiles for $a = 3$ mm with $\lambda = 120$ μm from (a) and $\lambda = 118.81$ μm from (b). (d) Profiles for $\theta = 5°$ and 15° for $a = 3$ mm and $\lambda = 120$ μm.

multiple lobes independently of the other modes, the detector records the incoherent superposition of these distributions. Figure 4(c) shows the profile of the resulting far-field distribution for a = 3 mm assuming two modes with different wavelengths of 120 and 118.81 μm, which represents the sum of the profile in Fig. 4(a) and the one indicated by the dashed line in Fig. 4(b). Because of the phase difference of about π between these two profiles, the oscillatory structure of Figs. 4(a) and 4(b) has almost completely disappeared in Fig. 4(c) so that the resulting far-field distribution is expected to be single lobed.

Apart from the coherence of the emitted radiation, the large divergence is the underlying fundamental property enabling the SIM. While the results of the calculations in Figs. 4(a)–4(c) were achieved assuming a divergence angle of θ = 34° as for Fig. 3, Fig. 4(d) shows the profile of the calculated far-field distributions for two smaller divergence angles of 5° and 15°. The other parameters are the same as in Fig. 4(a). The modulation of the profile is strongly reduced with decreasing divergence angle and completely disappears for θ = 5°. The physical reason for this dependence is that for a radiation field with a small divergence angle the first minimum of the profile occurs at an angle, where the intensity of the radiation field has already vanished.

Finally, we show how the SIM can be suppressed using an absorptive material (Eccosorb). In order to minimize the reflectivity of the absorber material, its absorption coefficient should be rather small and its thickness sufficiently large to avoid any transmission. We have chosen a thickness of 3 mm. However, the large thickness of the absorber makes it difficult to position it in such a way that the direct emission from the QCL can leave the cooling system and the radiation reflected at the out-coupling window of the cooling system is absorbed. Hence, the submount cannot be fully covered by the absorber. As a result, some modulation in the far-field distribution may still be observable. Figure 5(a) shows the corresponding setup with the QCL mounted at an angle of 20° with respect to the original setup. The absorber material is ring shaped so that the cold finger of the cooling system is completely covered with the absorber. The measured far-field distribution displayed in Fig. 5(b) is single lobed. Since the QCL is mounted at a finite angle, any residual radiation impinging on the submount is now deflected toward large positive angles and can no longer interfere with the directly emitted radiation.

The described mechanism does not only apply to THz QCLs with SP, but also to QCLs with metal-metal waveguides, for which the cases of cleaved and etched facets must be distinguished. This distinction is not applicable to THz QCLs with SP waveguides, which always have cleaved facets. In the case of cleaved facets, the modulations resulting from the reflections at the window are expected to appear in the lower half space (negative β), while the modulations resulting from interference between radiation from the front and the back facet develop predominantly in the upper half space. In the case of etched facets, the radiation is emitted predominantly into the upper half space (positive β), and the window usually reflects only a minor portion toward the submount/cold finger of the cooling system. Therefore, THz QCLs with metal-metal waveguides and cleaved facets are expected to exhibit similar phenomena as presented here for THz QCLs with SP waveguides.

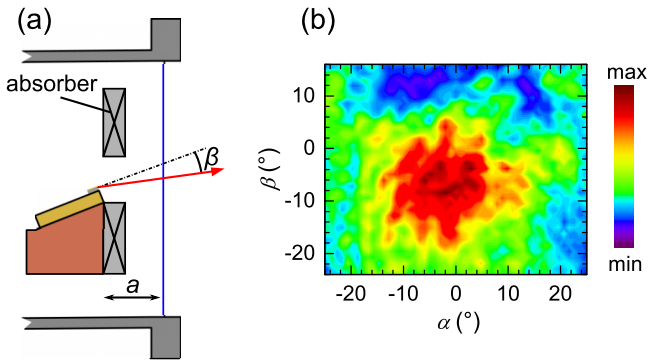

FIG. 5. (a) Setup using an absorptive material with the THz QCL mounted at an angle of 20°. (b) Measured far-field distribution for the setup shown in (a) using the 2.5-THz single-mode QCL.

In summary, we explained the appearance of multiple lobes in the far-field distribution of THz QCLs with single-plasmon waveguides by the interference of the directly emitted QCL radiation with radiation reflected at the window and the QCL submount/cold finger of the cooling system. As these parts are indispensable for the cryogenic operation of THz QCLs, the modulations of the far-field distribution reported in Refs. 14 and 15 may be explained in the same way. In Refs. 12 and 13, the modulations are observed in the upper half space in contrast to our observations. There are several possible reasons for this difference, which include a different mounting scheme of the QCL on the submount and additional reflecting surfaces within the cryostat. The identification of the mechanism and the presented model made it possible to suppress the modulation using an absorptive material and obtain a single-lobed far-field distribution.

We would like to thank R. Hey for sample growth, W. Anders for sample processing, and M. Hempel as well as P. Corfdir for a careful reading of the manuscript. The publication of this article was funded by the Open Access Fund of the Leibniz Association.

[1] N. Rothbart, H. Richter, M. Wienold, L. Schrottke, H. T. Grahn, and H.-W. Hübers, IEEE Trans. THz Sci. Technol. **3**, 617 (2013).
[2] P. Dean, A. Valavanis, J. Keeley, K. Bertling, Y. L. Lim, R. Alhathlool, A. D. Burnett, L. H. Li, S. P. Khanna, D. Indjin, T. Taimre, A. D. Rakić, E. H. Linfield, and A. G. Davies, J. Phys. D: Appl. Phys. **47**, 374008 (2014).
[3] M. Locatelli, M. Ravaro, S. Bartalini, L. Consolino, M. S. Vitiello, R. Cicchi, F. Pavone, and P. De Natale, Sci. Rep. **5**, 13566 (2015).
[4] T. Zhou, Z. Y. Tan, L. Gu, Z. L. Fu, Z. W. Yao, and J. C. Cao, Electron. Lett. **51**, 85 (2015).
[5] Y. Ren, J. N. Hovenier, R. Higgins, J. R. Gao, T. M. Klapwijk, S. C. Shi, A. Bell, B. Klein, B. S. Williams, S. Kumar, Q. Hu, and J. L. Reno, Appl. Phys. Lett. **97**, 161105 (2010).
[6] P. Dean, M. Salih, S. P. Khanna, L. H. Li, N. K. Saat, A. Valavanis, A. Burnett, J. E. Cunningham, A. G. Davies, and E. H. Linfield, Semicond. Sci. Technol. **27**, 094004 (2012).
[7] H.-W. Hübers, R. Eichholz, S. G. Pavlov, and H. Richter, J. Infrared Milli. Terahz. Waves **34**, 325 (2013).
[8] S. Bartalini, L. Consolino, P. Cancio, P. De Natale, P. Bartolini, A. Taschin, M. De Pas, H. Beere, D. Ritchie, M. S. Vitiello, and R. Torre, Phys. Rev. X **4**, 021006 (2014).
[9] H. Richter, M. Wienold, L. Schrottke, K. Biermann, H. T. Grahn, and H.-W. Hübers, IEEE Trans. THz Sci. Technol. **5**, 539 (2015).
[10] A. J. L. Adam, I. Kašalynas, J. N. Hovenier, T. O. Klaassen, J. R. Gao, E. E. Orlova, B. S. Williams, S. Kumar, Q. Hu, and J. L. Reno, Appl. Phys. Lett. **88**, 151105 (2006).
[11] E. E. Orlova, J. N. Hovenier, T. O. Klaassen, I. Kašalynas, A. J. L. Adam, J. R. Gao, T. Klapwijk, B. S. Williams, S. Kumar, Q. Hu, and J. L. Reno, Phys. Rev. Lett. **96**, 173904 (2006).
[12] M. Salih, P. Dean, A. Valavanis, S. P. Khanna, L. H. Li, J. E. Cunningham, A. G. Davies, and E. H. Linfield, J. Appl. Phys. **113**, 113110 (2013).
[13] H.-W. Hübers, S. G. Pavlov, A. D. Semenov, R. Köhler, L. Mahler, A. Tredicucci, H. E. Beere, D. A. Ritchie, and E. H. Linfield, Opt. Express **13**, 5890 (2005).
[14] E. Bründermann, M. Havenith, G. Scalari, M. Giovannini, J. Faist, J. Kunsch, L. Mechold, and M. Abraham, Opt. Express **14**, 1829 (2006).
[15] H. Richter, N. Rothbart, and H.-W. Hübers, J. Infrared Milli. Terahz. Waves **35**, 686 (2014).
[16] S. Barbieri, J. Alton, H. E. Beere, J. Fowler, E. H. Linfield, and D. A. Ritchie, Appl. Phys. Lett. **85**, 1674 (2004).
[17] M. Giehler, H. Kostial, R. Hey, and H. T. Grahn, Appl. Phys. Lett. **91**, 161102 (2007).
[18] B. E. A. Saleh and M. C. Teich, *Fundamentals of photonics*, 2nd ed. (Wiley, Hoboken, 2007).
[19] D. M. Pozar, *Microwave engineering*, 4th ed. (Wiley, Hoboken, 2012).